Report

Current Biology

The Structural Basis for Kinetochore Stabilization by Cnn1/CENP-T

Highlights

- Cryo-EM shows how the Ctf3c contacts Cnn1-Wip1
- Inner kinetochore assembly at yeast centromeres is not strictly hierarchical
- Microtubule contact modulates inner kinetochore assembly

Authors

Stephen M. Hinshaw,
Stephen C. Harrison

Correspondence

hinshaw@crystal.harvard.edu

In Brief

Connections between chromosomes and microtubules are provisional until all pairs of sister centromeres are properly attached to the metaphase spindle. Once this is achieved, the connections must persist until the end of anaphase. Hinshaw and Harrison report on a mechanism that solidifies kinetochores during anaphase, ensuring successful mitosis.

Hinshaw & Harrison, 2020, Current Biology *30*, 1–7
September 7, 2020
https://doi.org/10.1016/j.cub.2020.06.024

CellPress

Please cite this article in press as: Hinshaw and Harrison, The Structural Basis for Kinetochore Stabilization by Cnn1/CENP-T, Current Biology (2020), https://doi.org/10.1016/j.cub.2020.06.024

Current Biology

CellPress
OPEN ACCESS

Report

The Structural Basis for Kinetochore Stabilization by Cnn1/CENP-T

Stephen M. Hinshaw[1,2,*] and Stephen C. Harrison[1]
[1]Harvard Medical School, Howard Hughes Medical Institute, Boston, MA, USA
[2]Lead Contact
*Correspondence: hinshaw@crystal.harvard.edu
https://doi.org/10.1016/j.cub.2020.06.024

SUMMARY

Chromosome segregation depends on a regulated connection between spindle microtubules and centromeric DNA. The kinetochore mediates this connection and ensures it persists during anaphase, when sister chromatids must transit into daughter cells uninterrupted. The Ctf19 complex (Ctf19c) forms the centromeric base of the kinetochore in budding yeast. Biochemical experiments show that Ctf19c members associate hierarchically when purified from cell extract [1], an observation that is mostly explained by the structure of the complex [2]. The Ctf3 complex (Ctf3c), which is not required for the assembly of most other Ctf19c factors, disobeys the biochemical assembly hierarchy when observed in dividing cells that lack more basal components [3]. Thus, the biochemical experiments do not completely recapitulate the logic of centromeric Ctf19c assembly. We now present a high-resolution structure of the Ctf3c bound to the Cnn1-Wip1 heterodimer. Associated live-cell imaging experiments provide a mechanism for Ctf3c and Cnn1-Wip1 recruitment to the kinetochore. The mechanism suggests feedback regulation of Ctf19c assembly and unanticipated similarities in kinetochore organization between yeast and vertebrates.

RESULTS AND DISCUSSION

Reconstitution and Cryoelectron Microscopy Structure of the Ctf3c-Cnn1-Wip1 Complex

Most inner kinetochore proteins (those that assemble on centromeric DNA) belong to a large group of factors that associate biochemically. The group is called the Ctf19 complex (Ctf19c) in budding yeast and the constitutive centromere associated network (CCAN) in vertebrates [4–9]. Among Ctf19c sub-complexes, the last in the observed assembly hierarchy constitute a five-protein module containing the Ctf3 complex (Ctf3c, CENP-H/I/K in vertebrates) and the Cnn1-Wip1 heterodimer (CENP-T/W in vertebrates; Table S1). The presence of individual Ctf19c proteins varies across eukaryotic species, but where they have been observed, Cnn1-Wip1 homologs predict the existence of Ctf3 homologs [10].

We purified recombinant Ctf3c bound to Cnn1-Wip1 (Figure 1B) and determined its structure by cryoelectron microscopy (cryo-EM). Two-dimensional class averages show projected density that matches a previous reconstruction of the Ctf3c with additional density corresponding to Cnn1, Wip1, and the N-terminal part of Ctf3 (Figure 1C). Images from these class averages contributed to a final map resolved to a resolution of 3.2 Å for the full complex and to 3.1 Å for Ctf3-N, Wip1, and Cnn1 (Figure S1).

The two HEAT repeat domains of Ctf3 define a modular Ctf3c structure (Figure 2A). The N-terminal HEAT repeats (Ctf3-N) contact the C-terminal part of Mcm16/22 (Mcm16/22-C), and the C-terminal HEAT repeats (Ctf3-C) contact the N-terminal part of Mcm16/22 (Mcm16/22-N). The resolution is consistent throughout the map, with the exception of the extremities along the long axis of the complex due to subtle flexing at the midpoint.

Molecular Model of the Complete Ctf3c

The cryo-EM map enables modeling of the complete Ctf3c (Figure 2B). Previous studies have reported molecular structures of Ctf3-C with Mcm16/22-N from *S. cerevisiae* and of Ctf3-N with Mcm16/22-C from related yeast species [2, 13, 14]. In cryo-EM reconstructions of the complete Ctf19c, only the Ctf3-C module is well resolved [2, 15]. The new Ctf3c model shows how these structural modules relate to each other and provides a high-resolution model of *S. cerevisiae* Ctf3-N with Mcm16/22-C. Comparison with low-resolution reconstructions of the human homologs suggests the overall organization is conserved [16, 17].

The two Ctf3 HEAT repeat domains engage a discontinuous Mcm16/22 coiled-coil by distinct binding modes. The convex surface of Ctf3-N (Ctf3 1–223) interacts with Mcm16/22-C (Mcm16 148–181; Mcm22 142–239), and the concave inner surface contacts a two-helix underpinning motif (Ctf3 228–268). The concave surface of Ctf3-C (Ctf3 290–733) binds an extended Mcm16/22-N coiled-coil (Mcm16 81–134; Mcm22 69–128), with terminal helices of Mcm16/22-N (Mcm16 1–41; Mcm22 1–74) protruding and stabilizing a Ctf3 C-terminal helical knob [2]. Extended regions of Mcm16/22 lacking secondary structure but visible in the density (Mcm16 134–147; Mcm22 128–142) link the two Ctf3 HEAT modules (Figure 2C), which themselves are connected by an atypical HEAT repeat not previously visible (Ctf3 290–302).

Please cite this article in press as: Hinshaw and Harrison, The Structural Basis for Kinetochore Stabilization by Cnn1/CENP-T, Current Biology (2020), https://doi.org/10.1016/j.cub.2020.06.024

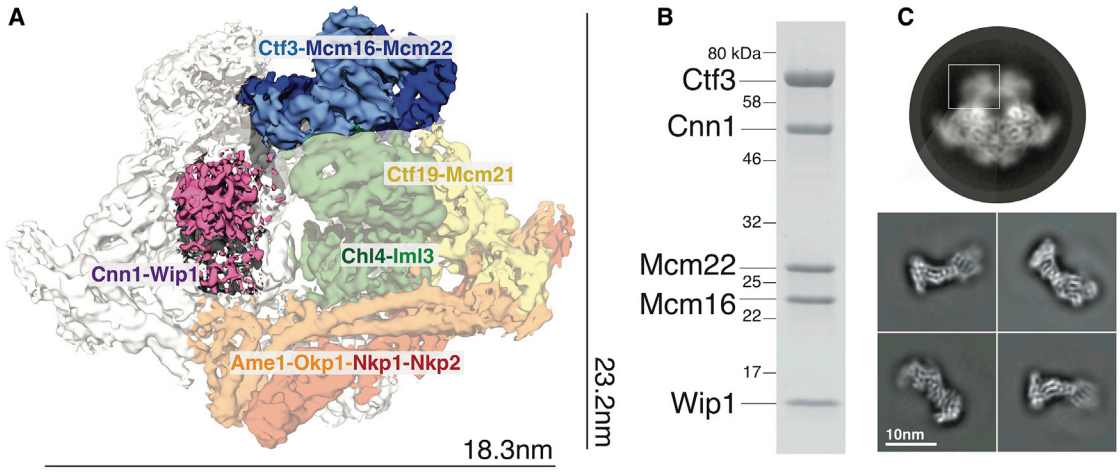

Figure 1. Reconstitution of the Ctf3c Bound to Cnn1-Wip1

(A) The structure of the dimeric Ctf19c with the five-protein Ctf3c-Cnn1-Wip1 complex highlighted. The Ctf19c density shows two copies of each protein subunit, and the unique protomer is colored according to subcomplex identity.

(B) The Ctf3c-Cnn1-Wip1 sample used for structure determination (SDS-PAGE; see also Tables S1 and S5).

(C) A representative two-dimensional class average showing the intact Ctf19c with the region corresponding to Ctf3c-Cnn1-Wip1 highlighted (top). Images below show two-dimensional class averages from the purified Ctf3c-Cnn1-Wip1 sample shown in (B).

See also Figure S1.

Observation and Validation of the Ctf3c-Cnn1 Interface

Cnn1 and Wip1 heterodimerize through complementary C-terminal histone folds. The Cnn1 histone fold contacts the Ctf3c through a histone fold extension motif (HFE) conserved among CENP-T proteins [1], and Cnn1-HFE mutants are defective in kinetochore localization. The Cnn1-HFE is well resolved in the density (Figure 3A). Previous work showed that contact between the Ctf3c and Cnn1 depends on a set of conserved residues in the Cnn1-HFE (Cnn1-E346, L350, and E351) [1]. Cnn1-L350 satisfies a hydrophobic pocket made by Ctf3-F142, and Cnn1-E351 caps the pocket by making contact with the backbone amide of Ctf3-S143. Cnn1-E346 does not make obvious contact with the Ctf3c. Together, Mcm22-R206 and Mcm22-R210 coordinate the negative charge of the Cnn1-E357 side chain, and Cnn1-S354 stabilizes this connection.

The Cnn1-Wip1 histone fold domain is sufficient to interact with the Ctf3c [1]. Mutation of Mcm22-R206 and R210 to alanine (Mcm22-2A) disrupted this interaction (Figure 3B). Analysis of amino acid conservation shows that the Cnn1 binding site is more conserved than the rest of the Ctf3c (Figure S2D). Mcm22-R210 aligns with basic amino acids (arginine or lysine) in most species examined (Figure 3C). A C-terminal appendage to the CENP-T HFE that is conserved in vertebrates, but not ordered in a previous CENP-T/W crystal structure [18], may also contribute to CENP-H/I/K binding in these species. The vertebrate CENP-T/W histone fold is sufficient to bind CENP-H/I/K/M [16, 19]. It also binds CENP-S/X to make a histone heterotetramer [18]. The current structure shows that both interactions could happen simultaneously, and this configuration enables known CENP-T/W/S/X-DNA contacts [20, 21]. Therefore, the mode of interaction between Cnn1-Wip1 and the Ctf3c is likely maintained throughout eukaryotes, although specific amino acid contacts may have shifted.

The Ctf3c and Cnn1-Wip1 Depend on Each Other for Kinetochore Recruitment

The Cnn1-HFE and a conserved N-terminal extension (Cnn1-N) (~270 amino acid residues) both contribute to Cnn1 kinetochore localization [11]. Cnn1-N contacts the microtubule lattice indirectly by binding the Spc24 and Spc25 components of the Ndc80 complex (Ndc80c) [12, 22, 23]. Cdc28/CDK1, Mps1, and Ipl1 all phosphorylate Cnn1-N and modulate its kinetochore recruitment [11, 24]. In particular, Mps1 inhibits Ndc80c binding by phosphorylating Cnn1-S74 [12].

To test the idea that Ctf19c assembly is hierarchical, we measured Cnn1 kinetochore localization in cells expressing Cnn1-3GFP (Figure 4A). Alignment of all measurements according to anaphase onset (determined by separation of Spc110-mCherry) shows that Cnn1 recruitment peaks in anaphase and dissipates as cells enter the next cell cycle (Figure 4B) [24]. If the Ctf3c is strictly required for Cnn1 localization, mutations that disrupt the Ctf3c-Cnn1 interaction should ablate Cnn1-3GFP localization. Instead, cells expressing Cnn1-3GFP and *mcm22-2A* lack the Cnn1 kinetochore signal until anaphase, when Cnn1 intensity peaks but does not reach wild-type levels. These cells are indistinguishable from *mcm22Δ* cells except that, unlike *mcm22Δ* cells, they are insensitive to the Mps1 inhibitor, cincreasin [25] (Figure S3B; two independent *mcm22Δ* isolates show modest sensitivity), indicating that Ctf3c functions unrelated to Cnn1-Wip1 recruitment are preserved. In a metaphase arrest, both mutants lack the robust Cnn1-3GFP kinetochore signal seen in a wild-type background (Figure S3C), showing that Cnn1 localization does not occur before anaphase in the mutants. Thus, the Ctf3c is required for Cnn1 localization until anaphase, when a second pathway for Cnn1 localization also contributes.

We also examined Ctf3-GFP localization using the same live-cell imaging method (Figure S3E). If the Ctf3c recruits

Please cite this article in press as: Hinshaw and Harrison, The Structural Basis for Kinetochore Stabilization by Cnn1/CENP-T, Current Biology (2020), https://doi.org/10.1016/j.cub.2020.06.024

CellPress
OPEN ACCESS

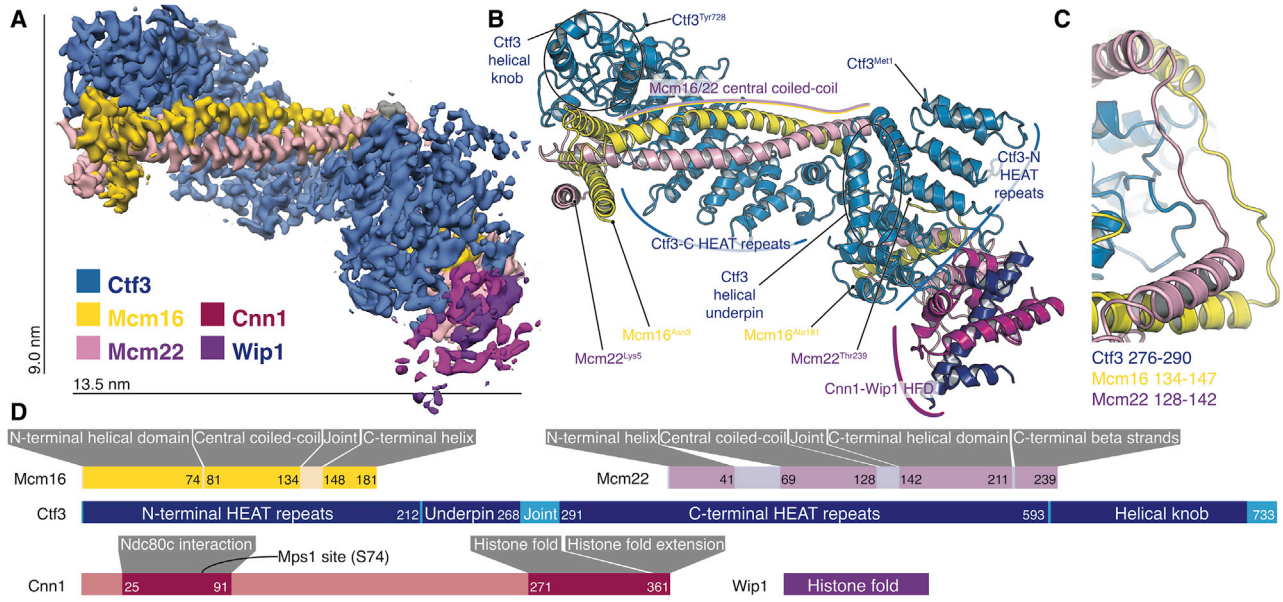

Figure 2. Structure of the Ctf3c Bound to Cnn1-Wip1

(A) cryo-EM map showing the Ctf3c bound to Cnn1-Wip1. The map is colored according to underlying protein subunit identity. See also Figures S1 and S2 and Table S2.

(B) Model of the Ctf3c bound to Cnn1-Wip1. See also Tables S3 and S5.

(C) Close-up view of the Ctf3c joint region that connects the Ctf3-N and Ctf3-C modules. Numbers are given for amino acid residues not contributing to the helical segments shown.

(D) Domain diagram describing the Ctf3c and Cnn1-Wip1. The Ndc80c-interacting region of Cnn1 contains an Mps1 phosphorylation site (Cnn1-S74) and corresponds to a previously described Spc24/Spc25 interaction sequence (SIS) [11, 12]. Dark colors indicate ordered regions. Light colors mark segments without defined secondary structure elements, including the joint region shown in (C).

Cnn1-Wip1 to kinetochores, as is the case in a strictly hierarchical Ctf19c assembly model, then mutations that perturb the Ctf3c-Cnn1 interaction should not affect Ctf3-GFP localization. In wild-type cells, the Ctf3-GFP signal at kinetochores dissipates after anaphase, although less dramatically than the Cnn1-3GFP signal (Figures 4C and 4D). Cells expressing Ctf3-GFP and *mcm22-2A* show diminished, but not ablated, Ctf3-GFP localization throughout the cell cycle, a phenotype indistinguishable from *cnn1Δ* cells. Therefore, the Ctf3c and Cnn1-Wip1 display reciprocally dependent localization: each requires the other for efficient recruitment to the kinetochore.

Residual Ctf3-GFP localization in *mcm22-2A* and *cnn1Δ* cells indicates that the Ctf3c contacts the kinetochore through a second interface. The structure of the Ctf19c shows that the Ctf3c contacts Ctf19-Mcm21 and Iml3, with the major contribution to Ctf3c localization coming from Ctf19-Mcm21 [2]. Ctf3-GFP localization in *ctf19Δ* cells is nearly undetectable until anaphase, when the Ctf3 kinetochore signal is comparable to that seen in wild-type cells (Figure 4C) [3]. This signal complements the one seen in *mcm22-2A* and *cnn1Δ* cells, suggesting there are two collaborating pathways for Ctf3c recruitment: one through Ctf19-Mcm21 and the other through Cnn1-Wip1. Indeed, in cells lacking both pathways (*ctf19Δ cnn1Δ* or *ctf19Δ mcm22-2A*), the Ctf3-GFP signal is completely absent from kinetochores (Figure 4D). Therefore, two pathways contribute to Ctf3c kinetochore localization, and the Cnn1-dependent pathway dominates during anaphase.

Implications for Regulated Kinetochore Assembly

Kinetochore assembly proceeds in stages according to the cell cycle. In vertebrates, CDK1 and PLK1 determine the timing of CENP-A nucleosome deposition [26, 27]. Ipl1/Aurora B and Ccd28/CDK1 determine the timing and extent of Ndc80 complex recruitment [28–33]. During anaphase, outer kinetochore proteins are enriched, ensuring a persistent connection to the depolymerizing filament [34, 35]. Ctf19c/CCAN factors link these regulated connections.

The structure of the complete Ctf3c-Cnn1-Wip1 assembly enables unambiguous placement of Cnn1-Wip1 relative to other Ctf19c components (Figure 4E). Poorly resolved regions of a previous Ctf19c cryo-EM map [2] accommodate the model presented here, with a 31 Å displacement of the Ctf3-N module at its tip (measured from Mcm22-D168; Figure S4A). The Mcm16/22 linker (Figure 2C) is the joint for the displacement. Cnn1-N, which is heavily phosphorylated *in vivo* [12, 24], projects toward the N-terminal helical domain of Ame1-Okp1. This implies a possible regulated contact, as has already been observed for Cse4-N and Ame1-Okp1 [2, 36]. The disordered N-terminal extensions of all four proteins cluster (Figure S4B), implying coordinated targeting by mitotic kinases. We previously observed that the Ctf3-N module must swing outward to accommodate the Cse4/CENP-A nucleosome [2]. The Mcm16/22 joint provides a mechanism for this flexing, and the proximity of Ame1-N, Okp1-N, Cse4-N, and Cnn1-N suggests that the flexing may be regulated.

Please cite this article in press as: Hinshaw and Harrison, The Structural Basis for Kinetochore Stabilization by Cnn1/CENP-T, Current Biology (2020), https://doi.org/10.1016/j.cub.2020.06.024

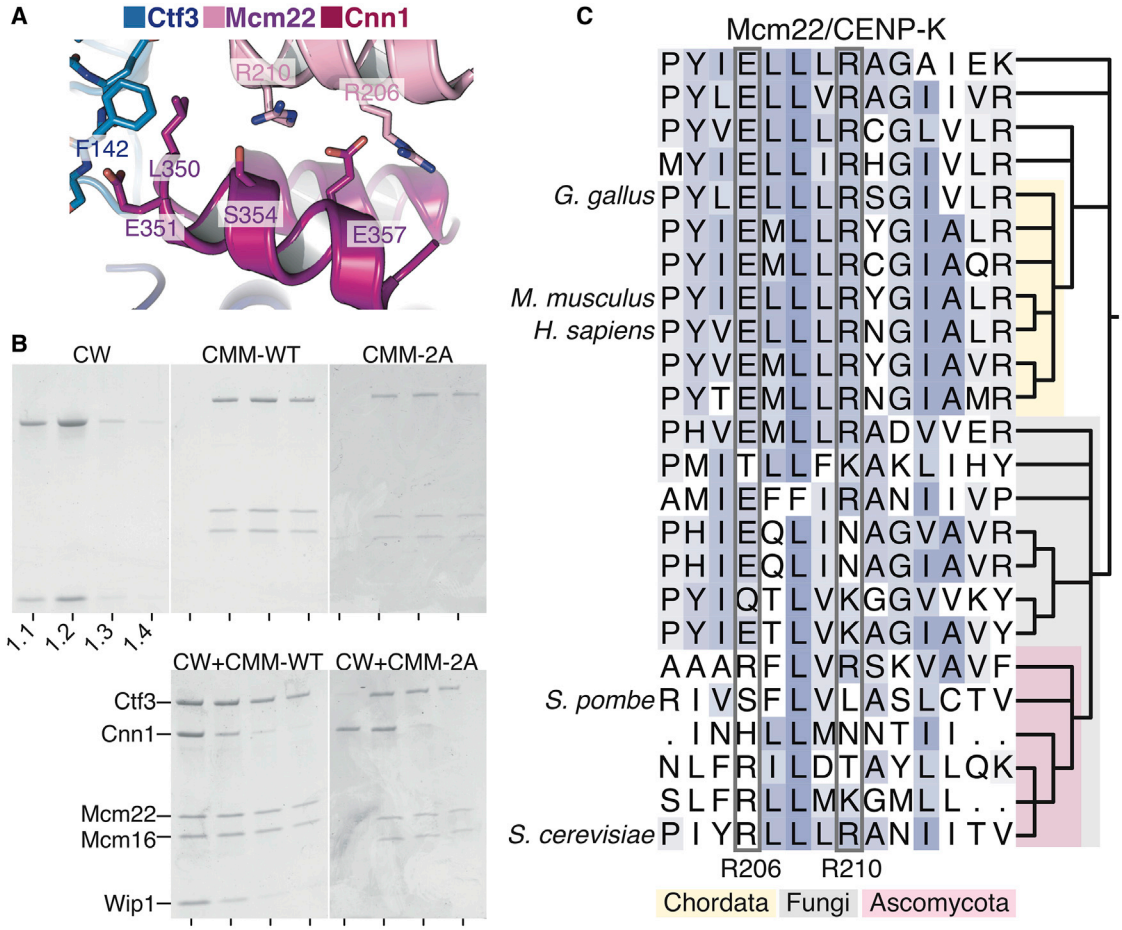

Figure 3. Observation and Validation of the Cnn1-Ctf3c Interface

(A) Close-up view of the Ctf3c-Cnn1 interface. The two Cnn1 helices shown constitute the Cnn1-HFE.

(B) Ctf3c binding to Cnn1-Wip1 and perturbation by the Mcm22-2A mutations. Equivalent gel filtration fractions are shown on each gel. The numbers beneath the first gel give the elution volume for each fraction in milliliters. The top panels show recombinant Cnn1-Wip1 (CW), Ctf3c (CMM), or Ctf3c containing the Mcm22-2A mutant protein (CMM-2A). The results of mixing with recombinant Cnn1-Wip1 are shown in the bottom panels. See also Table S5.

(C) Multiple sequence alignment showing Mcm22 conservation at the Cnn1 contact site. Evolutionary relationships for all included species are shown at right according to the NCBI Taxonomy Database.

See also Figure S2D.

The kinetochore loading of some Ctf19c proteins fluctuates during the cell cycle [24, 34]. This behavior is particularly pronounced for Cnn1; its recruitment depends on Ctf19c factors and is inhibited by Mps1 activity [11, 23, 24]. Precise inactivation of Ctf19c-dependent Cnn1 recruitment shows that two Cnn1 localization pathways operate independently. That the second pathway is only active during anaphase, when Mps1 is inactive [37], strongly suggests it requires Cnn1-Ndc80c-microtubule contact [11]. Cnn1 recruitment to kinetochore particles grown in the absence of microtubules depends totally on Mcm22, reinforcing this notion [38]. These observations imply complex feedback regulation: Mps1 activity inhibits Ctf19c-independent Cnn1 recruitment, and our findings show that this inhibition destabilizes Ctf3c kinetochore loading, further impairing Cnn1 recruitment. In vertebrate cells, Cnn1 binds the four-protein MIND complex upon phosphorylation by CDK1 [30, 32]. Although the CDK1 site is not obviously conserved in yeast, we cannot rule out that this or a related mechanism also contributes to Cnn1 localization. Restriction of Ctf19c-independent Cnn1 localization to anaphase suggests any such contribution must be Cdk1 independent. It remains to be seen how this regulatory logic has been modified in organisms that rely solely on the Cnn1/CENP-T pathway for kinetochore-microtubule contact [39].

Accumulated evidence suggests MIND-Ndc80c and Cnn1-Ndc80c are parallel connections between centromeric DNA and spindle microtubules (Figure 4F) [38, 40]. In vertebrate cells, mitotic kinases render the CENP-T connection dominant during anaphase [29]. CENP-A misincorporation is not sufficient for CENP-H recruitment to an ectopic chromosomal locus [41], implying that centromere-specific regulation is required for CCAN assembly. CENP-H and CENP-T are mutually required for robust localization [20]. Similarly, our observation of Cnn1-dependent Ctf3 localization demonstrates that regulated outer kinetochore assembly indirectly influences the stability of the Ctf19c and that, in yeast as in vertebrate cells, Cnn1-mediated kinetochore stabilization is most pronounced during anaphase.

Please cite this article in press as: Hinshaw and Harrison, The Structural Basis for Kinetochore Stabilization by Cnn1/CENP-T, Current Biology (2020), https://doi.org/10.1016/j.cub.2020.06.024

CellPress
OPEN ACCESS

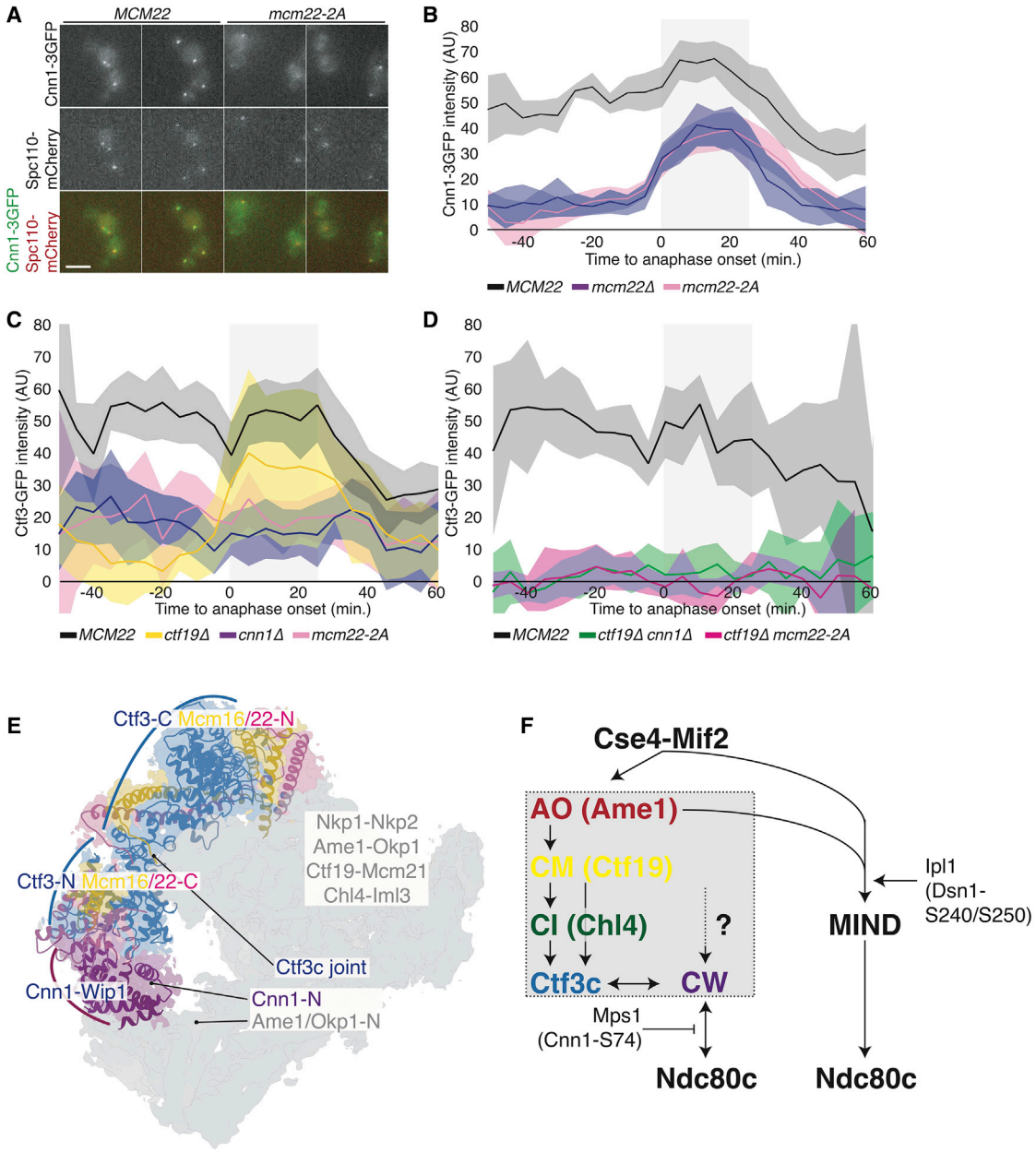

Figure 4. Live-Cell Imaging of Cnn1 and Ctf3 and Ctf19c Organization

(A) Representative micrographs showing cells expressing Cnn1-3GFP, Spc110-mCherry, and either Mcm22-wild type (WT) or Mcm22-2A. The same cells are shown at successive times during a single imaging session (scale bar, 5 μm). See Tables S4 and S5.

(B) Kinetochore-associated Cnn1-3GFP intensity in cells of the indicated genotypes (*MCM22*, SMH798; *mcm22Δ*, SMH805; *mcm22-2A*, SMH799). Shaded box denotes approximate duration of anaphase. Lines denote mean intensity values (shaded areas, 95% confidence intervals, at least 12 cells per curve).

(C) Kinetochore-associated Ctf3-GFP intensity shown as in (B) (*MCM22*, SMH728; *ctf19Δ*, SMH767; *cnn1Δ*, SMH768; *mcm22-2A*, SMH749). See also Figure S3.

(D) Kinetochore-associated Ctf3-GFP intensity shown as in (B) (*MCM22*, SMH728; *ctf19Δ cnn1Δ*, SMH783; *ctf19Δ mcm22-2A*, SMH784).

(E) Updated three-dimensional model of the Ctf19c showing newly determined positions of the Ctf3-N, Mcm16/22-C, Cnn1, and Wip1. Partially transparent cryo-EM density for a single Ctf19c protomer is shown [2]. The Ctf3c model was allowed to flex about its joint, bringing the Ctf3-N module (including Cnn1-Wip1) inward toward the Ame1/Okp1-N peptides. The Ctf3c joint and anchor points for flexible N-terminal extensions of Cnn1, Ame1, and Okp1 are indicated. See also Figure S4.

(F) An updated model for hierarchical Ctf19c assembly showing that the Ctf3c and Cnn1-Wip1 depend on each other for localization and Cnn1-Wip1 depends on Ndc80c interaction. The MIND-dependent pathway for centromere-microtubule contact is also shown. Ipl1 phosphorylates Dsn1, and Mps1 phosphorylates Cnn1 (AO, Ame1-Okp1; CM, Ctf19-Mcm21; CI, Chl4-Iml3; Ctf3c, Ctf3-Mcm16-Mcm22; CW, Cnn1-Wip1; MIND, Mtw1-Nntf1-Nsl1-Dsn1; Ndc80c, Ndc80-Nuf2-Spc24-Spc25).

STAR★METHODS

Detailed methods are provided in the online version of this paper and include the following:

- KEY RESOURCES TABLE
- RESOURCE AVAILABILITY
  - Lead contact
  - Materials Availability
  - Data and Code Availability
- EXPERIMENTAL MODEL AND SUBJECT DETAILS
  - Yeast strain generation and growth
- METHOD DETAILS
  - Protein purification and cryo-EM sample preparation
  - Cryo-EM data collection
  - Cryo-EM data processing and map determination
  - Molecular modeling
  - Fluorescence imaging and quantification
- QUANTIFICATION AND STATSITICAL ANALYSIS

SUPPLEMENTAL INFORMATION

Supplemental Information can be found online at https://doi.org/10.1016/j.cub.2020.06.024.

ACKNOWLEDGMENTS

We thank the staff at the Harvard Cryo-Electron Microscopy Center for Structural Biology for help with high-resolution cryo-EM data collection, particularly Richard Walsh and Sarah Sterling. We thank Shaun Rawson for real-time movie processing. We thank SBGrid for computational support, particularly Mick Timony and Justin O'Connor. We thank Jennifer Waters and the staff at the Nikon Imaging Center at Harvard Medical School for light microscopy support. We thank Adèle Marston and Huilin Zhou for comments on the manuscript. S.M.H. is an HHMI fellow of the Helen Hay Whitney Foundation. S.C.H. is an Investigator of the Howard Hughes Medical Institute.

AUTHOR CONTRIBUTIONS

S.M.H. conceived the study, performed the experiments, and wrote and edited the manuscript. S.C.H. supervised the work and edited the manuscript.

DECLARATION OF INTERESTS

The authors declare no competing interests.

Received: May 4, 2020
Revised: June 3, 2020
Accepted: June 5, 2020
Published: July 16, 2020

REFERENCES

1. Pekgöz Altunkaya, G., Malvezzi, F., Demianova, Z., Zimniak, T., Litos, G., Weissmann, F., Mechtler, K., Herzog, F., and Westermann, S. (2016). CCAN assembly configures composite binding interfaces to promote cross-linking of Ndc80 complexes at the kinetochore. Curr. Biol. *26*, 2370–2378.
2. Hinshaw, S.M., and Harrison, S.C. (2019). The structure of the Ctf19c/CCAN from budding yeast. eLife *8*, e44239.
3. Pot, I., Measday, V., Snydsman, B., Cagney, G., Fields, S., Davis, T.N., Muller, E.G., and Hieter, P. (2003). Chl4p and iml3p are two new members of the budding yeast outer kinetochore. Mol. Biol. Cell *14*, 460–476.
4. Cheeseman, I.M., Anderson, S., Jwa, M., Green, E.M., Kang, Js., Yates, J.R., 3rd, Chan, C.S., Drubin, D.G., and Barnes, G. (2002). Phospho-regulation of kinetochore-microtubule attachments by the Aurora kinase Ipl1p. Cell *111*, 163–172.
5. De Wulf, P., McAinsh, A.D., and Sorger, P.K. (2003). Hierarchical assembly of the budding yeast kinetochore from multiple subcomplexes. Genes Dev. *17*, 2902–2921.
6. Foltz, D.R., Jansen, L.E., Black, B.E., Bailey, A.O., Yates, J.R., 3rd, and Cleveland, D.W. (2006). The human CENP-A centromeric nucleosome-associated complex. Nat. Cell Biol. *8*, 458–469.
7. Izuta, H., Ikeno, M., Suzuki, N., Tomonaga, T., Nozaki, N., Obuse, C., Kisu, Y., Goshima, N., Nomura, F., Nomura, N., and Yoda, K. (2006). Comprehensive analysis of the ICEN (Interphase Centromere Complex) components enriched in the CENP-A chromatin of human cells. Genes Cells *11*, 673–684.
8. Okada, M., Cheeseman, I.M., Hori, T., Okawa, K., McLeod, I.X., Yates, J.R., 3rd, Desai, A., and Fukagawa, T. (2006). The CENP-H-I complex is required for the efficient incorporation of newly synthesized CENP-A into centromeres. Nat. Cell Biol. *8*, 446–457.
9. Westermann, S., Cheeseman, I.M., Anderson, S., Yates, J.R., 3rd, Drubin, D.G., and Barnes, G. (2003). Architecture of the budding yeast kinetochore reveals a conserved molecular core. J. Cell Biol. *163*, 215–222.
10. Plowman, R., Singh, N., Tromer, E.C., Payan, A., Duro, E., Spanos, C., Rappsilber, J., Snel, B., Kops, G.J.P.L., Corbett, K.D., and Marston, A.L. (2019). The molecular basis of monopolin recruitment to the kinetochore. Chromosoma *128*, 331–354.
11. Thapa, K.S., Oldani, A., Pagliuca, C., De Wulf, P., and Hazbun, T.R. (2015). The Mps1 kinase modulates the recruitment and activity of Cnn1(CENP-T) at Saccharomyces cerevisiae kinetochores. Genetics *200*, 79–90.
12. Malvezzi, F., Litos, G., Schleiffer, A., Heuck, A., Mechtler, K., Clausen, T., and Westermann, S. (2013). A structural basis for kinetochore recruitment of the Ndc80 complex via two distinct centromere receptors. EMBO J. *32*, 409–423.
13. Hu, L., Huang, H., Hei, M., Yang, Y., Li, S., Liu, Y., Dou, Z., Wu, M., Li, J., Wang, G.Z., et al. (2019). Structural analysis of fungal CENP-H/I/K homologs reveals a conserved assembly mechanism underlying proper chromosome alignment. Nucleic Acids Res. *47*, 468–479.
14. Zhang, Y., Zhao, C., Cao, B., Ye, J., Huang, H., Hu, L., Tian, W., and He, X. (2020). Structural insights into the intramolecular interactions of centromere protein CENP-I. J. Mol. Recognit. *33*, e2837.
15. Yan, K., Yang, J., Zhang, Z., McLaughlin, S.H., Chang, L., Fasci, D., Ehrenhofer-Murray, A.E., Heck, A.J.R., and Barford, D. (2019). Structure of the inner kinetochore CCAN complex assembled onto a centromeric nucleosome. Nature *574*, 278–282.
16. Basilico, F., Maffini, S., Weir, J.R., Prumbaum, D., Rojas, A.M., Zimniak, T., De Antoni, A., Jeganathan, S., Voss, B., van Gerwen, S., et al. (2014). The pseudo GTPase CENP-M drives human kinetochore assembly. eLife *3*, e02978.
17. Pesenti, M.E., Prumbaum, D., Auckland, P., Smith, C.M., Faesen, A.C., Petrovic, A., Erent, M., Maffini, S., Pentakota, S., Weir, J.R., et al. (2018). Reconstitution of a 26-subunit human kinetochore reveals cooperative microtubule binding by CENP-OPQUR and NDC80. Mol. Cell *71*, 923–939.e10.
18. Nishino, T., Takeuchi, K., Gascoigne, K.E., Suzuki, A., Hori, T., Oyama, T., Morikawa, K., Cheeseman, I.M., and Fukagawa, T. (2012). CENP-T-W-S-X forms a unique centromeric chromatin structure with a histone-like fold. Cell *148*, 487–501.
19. McKinley, K.L., Sekulic, N., Guo, L.Y., Tsinman, T., Black, B.E., and Cheeseman, I.M. (2015). The CENP-L-N complex forms a critical node in an integrated meshwork of interactions at the centromere-kinetochore interface. Mol. Cell *60*, 886–898.
20. Hori, T., Amano, M., Suzuki, A., Backer, C.B., Welburn, J.P., Dong, Y., McEwen, B.F., Shang, W.H., Suzuki, E., Okawa, K., et al. (2008). CCAN

makes multiple contacts with centromeric DNA to provide distinct pathways to the outer kinetochore. Cell *135*, 1039–1052.

21. Takeuchi, K., Nishino, T., Mayanagi, K., Horikoshi, N., Osakabe, A., Tachiwana, H., Hori, T., Kurumizaka, H., and Fukagawa, T. (2014). The centromeric nucleosome-like CENP-T-W-S-X complex induces positive supercoils into DNA. Nucleic Acids Res. *42*, 1644–1655.
22. Nishino, T., Rago, F., Hori, T., Tomii, K., Cheeseman, I.M., and Fukagawa, T. (2013). CENP-T provides a structural platform for outer kinetochore assembly. EMBO J. *32*, 424–436.
23. Schleiffer, A., Maier, M., Litos, G., Lampert, F., Hornung, P., Mechtler, K., and Westermann, S. (2012). CENP-T proteins are conserved centromere receptors of the Ndc80 complex. Nat. Cell Biol. *14*, 604–613.
24. Bock, L.J., Pagliuca, C., Kobayashi, N., Grove, R.A., Oku, Y., Shrestha, K., Alfieri, C., Golfieri, C., Oldani, A., Dal Maschio, M., et al. (2012). Cnn1 inhibits the interactions between the KMN complexes of the yeast kinetochore. Nat. Cell Biol. *14*, 614–624.
25. Dorer, R.K., Zhong, S., Tallarico, J.A., Wong, W.H., Mitchison, T.J., and Murray, A.W. (2005). A small-molecule inhibitor of Mps1 blocks the spindle-checkpoint response to a lack of tension on mitotic chromosomes. Curr. Biol. *15*, 1070–1076.
26. McKinley, K.L., and Cheeseman, I.M. (2014). Polo-like kinase 1 licenses CENP-A deposition at centromeres. Cell *158*, 397–411.
27. Silva, M.C., Bodor, D.L., Stellfox, M.E., Martins, N.M., Hochegger, H., Foltz, D.R., and Jansen, L.E. (2012). Cdk activity couples epigenetic centromere inheritance to cell cycle progression. Dev. Cell *22*, 52–63.
28. Akiyoshi, B., Nelson, C.R., and Biggins, S. (2013). The aurora B kinase promotes inner and outer kinetochore interactions in budding yeast. Genetics *194*, 785–789.
29. Hara, M., Ariyoshi, M., Okumura, E.I., Hori, T., and Fukagawa, T. (2018). Multiple phosphorylations control recruitment of the KMN network onto kinetochores. Nat. Cell Biol. *20*, 1378–1388.
30. Huis In 't Veld, P.J., Jeganathan, S., Petrovic, A., Singh, P., John, J., Krenn, V., Weissmann, F., Bange, T., and Musacchio, A. (2016). Molecular basis of outer kinetochore assembly on CENP-T. eLife *5*, e21007.
31. Kim, S., and Yu, H. (2015). Multiple assembly mechanisms anchor the KMN spindle checkpoint platform at human mitotic kinetochores. J. Cell Biol. *208*, 181–196.
32. Rago, F., Gascoigne, K.E., and Cheeseman, I.M. (2015). Distinct organization and regulation of the outer kinetochore KMN network downstream of CENP-C and CENP-T. Curr. Biol. *25*, 671–677.
33. Suzuki, A., Badger, B.L., and Salmon, E.D. (2015). A quantitative description of Ndc80 complex linkage to human kinetochores. Nat. Commun. *6*, 8161.
34. Dhatchinamoorthy, K., Shivaraju, M., Lange, J.J., Rubinstein, B., Unruh, J.R., Slaughter, B.D., and Gerton, J.L. (2017). Structural plasticity of the living kinetochore. J. Cell Biol. *216*, 3551–3570.
35. Gascoigne, K.E., and Cheeseman, I.M. (2013). CDK-dependent phosphorylation and nuclear exclusion coordinately control kinetochore assembly state. J. Cell Biol. *201*, 23–32.
36. Anedchenko, E.A., Samel-Pommerencke, A., Tran Nguyen, T.M., Shahnejat-Bushehri, S., Pöpsel, J., Lauster, D., Herrmann, A., Rappsilber, J., Cuomo, A., Bonaldi, T., and Ehrenhofer-Murray, A.E. (2019). The kinetochore module Okp1^{CENP-Q}/Ame1^{CENP-U} is a reader for N-terminal modifications on the centromeric histone Cse4^{CENP-A}. EMBO J. *38*, e98991.
37. Palframan, W.J., Meehl, J.B., Jaspersen, S.L., Winey, M., and Murray, A.W. (2006). Anaphase inactivation of the spindle checkpoint. Science *313*, 680–684.
38. Lang, J., Barber, A., and Biggins, S. (2018). An assay for de novo kinetochore assembly reveals a key role for the CENP-T pathway in budding yeast. eLife *7*, e37819.
39. Cortes-Silva, N., Ulmer, J., Kiuchi, T., Hsieh, E., Cornilleau, G., Ladid, I., Dingli, F., Loew, D., Katsuma, S., and Drinnenberg, I.A. (2020). CenH3-independent kinetochore assembly in Lepidoptera requires CCAN, including CENP-T. Curr. Biol. *30*, 561–572.e10.
40. Hara, M., and Fukagawa, T. (2020). Dynamics of kinetochore structure and its regulations during mitotic progression. Cell. Mol. Life Sci. Published online February 12, 2020. https://doi.org/10.1007/s00018-020-03472-4.
41. Gascoigne, K.E., Takeuchi, K., Suzuki, A., Hori, T., Fukagawa, T., and Cheeseman, I.M. (2011). Induced ectopic kinetochore assembly bypasses the requirement for CENP-A nucleosomes. Cell *145*, 410–422.
42. Mastronarde, D.N. (2005). Automated electron microscope tomography using robust prediction of specimen movements. J. Struct. Biol. *152*, 36–51.
43. Zheng, S.Q., Palovcak, E., Armache, J.P., Verba, K.A., Cheng, Y., and Agard, D.A. (2017). MotionCor2: anisotropic correction of beam-induced motion for improved cryo-electron microscopy. Nat. Methods *14*, 331–332.
44. Rohou, A., and Grigorieff, N. (2015). CTFFIND4: Fast and accurate defocus estimation from electron micrographs. J. Struct. Biol. *192*, 216–221.
45. Zivanov, J., Nakane, T., Forsberg, B.O., Kimanius, D., Hagen, W.J., Lindahl, E., and Scheres, S.H. (2018). New tools for automated high-resolution cryo-EM structure determination in RELION-3. eLife *7*, e42166.
46. Kucukelbir, A., Sigworth, F.J., and Tagare, H.D. (2014). Quantifying the local resolution of cryo-EM density maps. Nat. Methods *11*, 63–65.
47. Pettersen, E.F., Goddard, T.D., Huang, C.C., Couch, G.S., Greenblatt, D.M., Meng, E.C., and Ferrin, T.E. (2004). UCSF Chimera–a visualization system for exploratory research and analysis. J. Comput. Chem. *25*, 1605–1612.
48. Emsley, P., Lohkamp, B., Scott, W.G., and Cowtan, K. (2010). Features and development of Coot. Acta Crystallogr. D Biol. Crystallogr. *66*, 486–501.
49. Afonine, P.V., Poon, B.K., Read, R.J., Sobolev, O.V., Terwilliger, T.C., Urzhumtsev, A., and Adams, P.D. (2018). Real-space refinement in PHENIX for cryo-EM and crystallography. Acta Crystallogr. D Struct. Biol. *74*, 531–544.
50. Katoh, K., Rozewicki, J., and Yamada, K.D. (2019). MAFFT online service: multiple sequence alignment, interactive sequence choice and visualization. Brief. Bioinform. *20*, 1160–1166.
51. Waterhouse, A.M., Procter, J.B., Martin, D.M., Clamp, M., and Barton, G.J. (2009). Jalview Version 2–a multiple sequence alignment editor and analysis workbench. Bioinformatics *25*, 1189–1191.
52. Waterhouse, A., Bertoni, M., Bienert, S., Studer, G., Tauriello, G., Gumienny, R., Heer, F.T., de Beer, T.A.P., Rempfer, C., Bordoli, L., et al. (2018). SWISS-MODEL: homology modelling of protein structures and complexes. Nucleic Acids Res. *46* (W1), W296–W303.
53. Schindelin, J., Arganda-Carreras, I., Frise, E., Kaynig, V., Longair, M., Pietzsch, T., Preibisch, S., Rueden, C., Saalfeld, S., Schmid, B., et al. (2012). Fiji: an open-source platform for biological-image analysis. Nat. Methods *9*, 676–682.
54. Ashkenazy, H., Abadi, S., Martz, E., Chay, O., Mayrose, I., Pupko, T., and Ben-Tal, N. (2016). ConSurf 2016: an improved methodology to estimate and visualize evolutionary conservation in macromolecules. Nucleic Acids Res. *44* (W1), W344–W350.
55. Longtine, M.S., Fares, H., and Pringle, J.R. (1998). Role of the yeast Gin4p protein kinase in septin assembly and the relationship between septin assembly and septin function. J. Cell Biol. *143*, 719–736.
56. Suhandynata, R.T., Quan, Y., Yang, Y., Yuan, W.T., Albuquerque, C.P., and Zhou, H. (2019). Recruitment of the Ulp2 protease to the inner kinetochore prevents its hyper-sumoylation to ensure accurate chromosome segregation. PLoS Genet. *15*, e1008477.
57. van Hooff, J.J., Tromer, E., van Wijk, L.M., Snel, B., and Kops, G.J. (2017). Evolutionary dynamics of the kinetochore network in eukaryotes as revealed by comparative genomics. EMBO Rep. *18*, 1559–1571.

Please cite this article in press as: Hinshaw and Harrison, The Structural Basis for Kinetochore Stabilization by Cnn1/CENP-T, Current Biology (2020), https://doi.org/10.1016/j.cub.2020.06.024

STAR★METHODS

KEY RESOURCES TABLE

REAGENT or RESOURCE	SOURCE	IDENTIFIER
Antibodies		
anti-FLAG-HRP (from ascites)	Abcam	49763
anti-PGK1 (mouse monoclonal)	Invitrogen	459250
goat anti-mouse-IgG-HRP (rabbit polyclonal)	Abcam	97046
Bacterial and Virus Strains		
Rosetta 2(DE3)pLysS; *E. coli*	EMD Millipore	71403
Chemicals, Peptides, and Recombinant Proteins		
Concanavilin A	Sigma	C2010
Synthetic complete medium	Sunrise Science	1300-030
Cincreasin (6-bromo-1,3-benzoxazol-2(3h)-one)	Fisher	19932-85-5
Deposited Data		
Ctf3-Mcm16-Mcm22-Cnn1-Wip1 cryo-EM map	This paper	EMD-21910
Ctf3-Mcm16-Mcm22-Cnn1-Wip1 model	This paper	PDB 6WUC
Experimental Models: Cell Lines		
High Five cells; *Trichoplusia ni*	ThermoFisher	B85502
Experimental Models: Organisms/Strains		
Budding yeast strains (W303 and S288c)	This paper	See Table S4
Recombinant DNA		
Plasmids used in this work	This paper	See Table S5
Software and Algorithms		
SerialEM (v3.7)	[42]	https://bio3d.colorado.edu/SerialEM/
MotionCor2 (v1.1.0)	[43]	https://emcore.ucsf.edu/ucsf-motioncor2
CTFFIND4 (v4.1.8)	[44]	https://grigoriefflab.umassmed.edu/ctffind4
Relion (v3.0.1)	[45]	https://www3.mrc-lmb.cam.ac.uk/relion/
ResMap (v1.1.4)	[46]	http://resmap.sourceforge.net/
PyMol (v2.3.2)	Schrödinger, LLC	https://pymol.org/2/
Chimera (v.1.14.0)	[47]	https://www.cgl.ucsf.edu/chimera/
Coot (v0.8.8)	[48]	https://www2.mrc-lmb.cam.ac.uk/personal/pemsley/coot/
Phenix (v1.17.1)	[49]	https://www.phenix-online.org/
MAFFT	[50]	https://mafft.cbrc.jp/alignment/software/
JalView	[51]	http://www.jalview.org/
SWISS-MODEL	[52]	https://swissmodel.expasy.org/
Fiji	[53]	https://imagej.net/Fiji
Python 2.7.2		https://www.python.org/
ConSurf server	[54]	https://consurf.tau.ac.il/
Prism v8.4.1	GraphPad	https://www.graphpad.com/scientific-software/prism/
Other		
C-flat holey carbon grids	EMS	CF-2/1-4C

RESOURCE AVAILABILITY

Lead contact

Further information and requests for resources and reagents should be directed to and will be fulfilled by the Lead Contact, Stephen M. Hinshaw (hinshaw@crystal.harvard.edu).

Please cite this article in press as: Hinshaw and Harrison, The Structural Basis for Kinetochore Stabilization by Cnn1/CENP-T, Current Biology (2020), https://doi.org/10.1016/j.cub.2020.06.024

Materials Availability

Plasmids and budding yeast strains used in this study are listed in the Key Resources Table and associated Supplemental Tables. Requests will be fulfilled by the Lead Contact.

Data and Code Availability

The accession numbers for the cryo-EM structure reported in this paper are EMD-21910 (map) and PDB 6WUC (model) and have been deposited in the EMDB and PDB, respectively.

EXPERIMENTAL MODEL AND SUBJECT DETAILS

Yeast strain generation and growth

Yeast strains used in this study are listed in Table S4. Strains were grown in rich medium with additives as indicated or in dropout medium (synthetic complete (SC), Sunrise Science Products) as required. Cincreasin (6-bromo-1,3-benzoxazol-2(3h)-one, Fisher Scientific) was diluted to 100 mM in DMSO immediately before use as described previously [25]. Benomyl (10 mg/mL stock solution in DMSO) was mixed with near-boiling medium to prevent crystallization. For metaphase arrests, cells were grown as for other imaging experiments (below) and arrested by addition of 10 μg/ml benomyl and 15 μg/ml nocodazole. After one hour, benomyl was re-added at the same concentration. Cells were imaged as described below two hours after the arrest was initiated.

The Cnn1-3GFP Spc110-mCherry strain was a generous gift from Peter De Wulf [24]. Derivatives were generated by lithium acetate-mediated integration of PCR products [55]. Ctf3-GFP Spc110-mCherry strains were generated similarly, except *ctf19Δ mcm22-2A* and *ctf19d cnn1Δ* strains were created by mating of the individual mutants in the imaging background and subsequent sporulation. Western blotting was carried out as described [2] with the following antibodies: anti-FLAG-HRP (Abcam 49763 from ascites), anti-PGK1 (Invitrogen 459250), and rabbit anti-mouse IgG-HRP (Abcam 97046).

METHOD DETAILS

Protein purification and cryo-EM sample preparation

Recombinant kinetochore proteins were purified as described previously and stored as aliquots at −80°C [2]. To reconstitute the sample used for cryo-EM, equimolar amounts of purified Ctf3c and Cnn1-Wip1 were mixed and incubated on ice for one hour before injection onto a size exclusion column (Superdex 200 Increase 5/150 GL) developed in gel filtration buffer (20 mM Tris-HCl, pH 8.5; 150 mM NaCl, 1 mM EDTA; 1 mM TCEP; 0.02% Na-azide (*w:v*)). The sample was eluted by isocratic flow at 0.1 mL/min, and fractions were collected at 30 s intervals. For the sample reported here, excess recombinant NH_2-biotin-Ulp2-CCR peptide [56] was included but not visualized in the final density.

After verification of complex formation by SDS-PAGE, the purified sample was vitrified for cryo-EM. 3.5 μL of gel filtration column eluate (∼0.5 mg/ml) was applied to a holey carbon support (Quantifoil 2/1-4Cu-50) at ∼90% relative humidity. The grid was immediately blotted on both sides for four seconds and plunged into liquid ethane (Gatan CryoPlunge 3).

Cryo-EM data collection

Data collection is described in Table S2 and was done as described previously [2] using SerialEM [42]. A Titan Krios G3i (Gatan) operating at 300 kV was used to illuminate the sample with a 1 μm beam in nanoprobe mode with a pre-camera energy filter (Gatan) slit width of 100 eV. Movies were collected on a K3 detector (Gatan) in counting mode with a pixel size of 0.825 μm. 50 frames were collected per 3 s movie, with a total dose of 60 electrons/$Å^2$ divided equally among the frames. The defocus range was set between −1.2 and −3.0 μm. Using image shift and real-time coma-correction by beam tilt as implemented in SerialEM, nine holes were visited at each stage position, and five movies were taken per hole, giving a total of 45 movies per stage movement.

Cryo-EM data processing and map determination

Initial movie processing steps were carried out using an in-house pipeline (Shaun Rawson) built upon RELION-3.0 software [45]. Movies, stored as LZW-compressed tiffs, were aligned using MotionCorr2 (5-by-5 patches) [43], and CTFFIND4 was used for CTF parameter estimation [44]. All subsequent processing steps were carried out in Relion 3.0 after data collection. Micrographs were discarded if the maximum resolution estimation (CTFFIND4) was worse than 4 Å. Data processing steps are given in detail in Figure S1. Care was taken after 2D-classification to select only projections showing features corresponding to the Ctf3-N module, and this proved essential for generating a high-quality map of the complete complex. Map quality and mask appropriateness were assessed visually in Chimera [47]. ResMap was used to estimate local resolution throughout the map [46].

Molecular modeling

Deposited coordinates describing Ctf3-C module (PDB: 6OUA) [2] was used as a starting model for the corresponding part of the density. Minor modifications were required, including updates to disordered segments between HEAT repeats and parts of the Ctf3 helical knob. The C-terminal-most alpha helical segment of Ctf3 is also well-ordered in the current model, whereas it was poorly represented in the previous map. We used SWISS-MODEL [52] to generate a homology model of *S. cerevisiae* Ctf3-N from a crystal structure of this domain from *Chaetomium thermophilum* (PDB: 5Z07) [13]. Mcm16/22-C and their connections to Mcm16/22-N were

Please cite this article in press as: Hinshaw and Harrison, The Structural Basis for Kinetochore Stabilization by Cnn1/CENP-T, Current Biology (2020), https://doi.org/10.1016/j.cub.2020.06.024

built *de novo*. A homology model for the Cnn1-Wip1 histone fold domain was constructed similarly using a crystal structure of the chicken homologs (PDB: 3B0C) [18]. The homology models were docked into the cryo-EM density using Chimera v1.14.0 and modified using COOT v0.8.8 [47, 48]. The map showing the Cff3-N module was used for adjusting the corresponding atomic coordinates in later stages of model building. Phenix v1.17.1 Real Space Refine [49] was used as a final step to optimize model geometry. The final model is described in Table S3. All automated refinements and model statistics calculations were done using the map of the full complex.

For analysis of amino acid conservation, multiple sequence alignments were created with MAFFT and displayed with JalView [50, 51]. Surface rendering showing amino acid conservation was generated by the ConSurf server [54]. Inputs for multiple sequence alignments were taken from van Hooff and modified if necessary [57].

Fluorescence imaging and quantification

Saturated overnight cultures of the indicated strains were grown in SCA (SC supplemented with 20 μg/ml additional adenine). Cultures were diluted 1:50 (*v:v*) into new SCA and grown at least four hours longer before mounting on concanavalin A-coated coverslips for imaging. Coverslips were mounted in a humidified chamber heated to ~29°C using a Tokai Hit stage-top incubator.

Images were taken with NIS-Elements acquisition software used to run a Nikon Ti2 motorized inverted microscope with the Perfect Focus System, a Lumencor SpectraX fluorescence light source, a Nikon Plan Apo 60x NA objective, and a Hamamatsu Flash4.0 V2+ sCMOS camera. Optical paths were: GFP – SpectraX Cyan (illumination), Lumencor 470/24 (excitation), and Semrock FF03 525/50 (emission); mCherry – SpectraX GreenYellow (illumination), Lumencor 525/25 (excitation), and Semrock FF02 641/75 (emission). Nine z-heights (0.4 μm spacing) were taken per stage position. Time points were taken at five-minute intervals for at least two hours for each imaging session.

Maximum z-projections for each time point were analyzed for five stage positions for each indicated strain. To get intensity values, a 6 pixel circle (~.65 μm diameter) was drawn around a single kinetochore cluster, and background signal in an adjacent nuclear region was subtracted for each time point using Fiji [53]. Irreversible Spc110-mCherry separation was taken as an indication of anaphase initiation. *ctf19Δ* cells show pronounced and prolonged Spc110 separation before anaphase initiation due to inefficient sister centromere cohesion, and care was taken to differentiate this from bona fide anaphase initiation. At least 12 cells were included for each measurement displayed. All traces shown on the same plot originated from the same experiment. Plots were generated with GraphPad Prism v8.4.1 software (GraphPad). Experiments were repeated at least twice for the indicated genotypes with equivalent results. Imaging conditions were kept constant for all experiments, although the GFP illumination time differed for Ctf3-GFP and Cnn1-3GFP strains.

QUANTIFICATION AND STATSITICAL ANALYSIS

Statistical analysis for cryo-EM structure determination was performed as described. The Phenix component Mtriage was used to compute the model parameters, its fit to the density, and to generate a final resolution measurement from half-maps. All statistical analyses for live-cell imaging experiments are described in corresponding figure legends and performed with GraphPad Prism software.